Supporting Information for:

Olsalazine-Based Metal–Organic Frameworks as Biocompatible Platforms for H_2 Adsorption and Drug Delivery

*Dana J. Levine, Tomče Runčevski, Matthew T. Kapelewski, Benjamin K. Keitz, Julia Oktawiec, Douglas A. Reed, Jarad A. Mason, Henry Z. H. Jiang, Kristen A. Colwell, Christina Legendre, Stephen A. FitzGerald, Jeffrey R. Long**

* Email: jrlong@berkeley.edu

Journal of the American Chemical Society

Table of Contents

I. Synthesis and Characterization

Scheme S1. Synthesis of olsalazine acid (H_4olz).

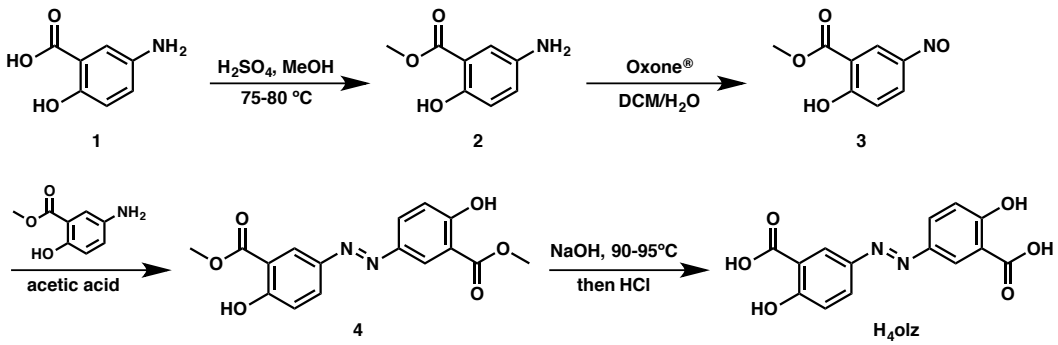

*Methyl 5-aminosalicylate (**2**)*. 5-Amino salicylic acid (**1**, 20.0 g, 131 mmol) was suspended in methanol (250 mL). Concentrated sulfuric acid (10 mL) was added, and the solution was heated to reflux (75-80 °C) with stirring. The solution was kept at reflux overnight, then cooled to ambient temperature and concentrated on a rotary evaporator. The resulting pale lavender powder was treated by slow addition of saturated sodium bicarbonate (500 mL). The product was extracted with 3×200 mL portions of ethyl acetate. The organic layers were combined and dried over magnesium sulfate, filtered, then concentrated on a rotary evaporator. The residue was dried under vacuum to give the title compound as a light tan solid (10.7 g, 49.2% yield).

*Methyl 5-nitrososalicylate (**3**)*. To a solution of compound **2** (3.01 g, 18.0 mmol) in CH_2Cl_2 (75 mL), a solution of Oxone (11.1 g, 18.0 mmol) in H_2O (75 mL) was added. The biphasic mixture was stirred vigorously at room temperature, as the CH_2Cl_2 layer developed a dark green color. The progression of the reaction was monitored by LCMS until the starting material was fully consumed (usually about two hours). The layers were separated, then the aqueous layer was washed with additional CH_2Cl_2 (2 × 75 mL). The combined organic layers were filtered through a short silica column, eluting with CH_2Cl_2. The filtrate was concentrated on a rotary evaporator and dried under vacuum to afford the title compound as a bright green solid (1.69 g). Some over-oxidation of nitroso to nitro was evident by LCMS. However, this did not interfere with the subsequent reaction, and the crude mixture was used in the next step without further purification.

*Olsalazine methyl ester (**4**)*. The crude mixture obtained from the previous step was dissolved in acetic acid (35 mL). To this was added a solution of **2** (1.50 g, 9 mmol) in acetic acid (35 mL). The reaction mixture was stirred at room temperature overnight. The resulting precipitate was collected on a Buchner funnel and washed sequentially with acetic acid and water to afford **4** as a bright yellow solid (1.78 g, 29.9% yield, two steps).

Olsalazine acid (H_4olz). Compound **4** (1.75 g, 5.30 mmol) was dissolved in 50 mL aqueous NaOH (1.06 g, 26.5 mmol). The deep red solution was heated to reflux (90-95 °C) with stirring. After 2 h, the reaction mixture was allowed to cool to ambient temperature. Concentrated HCl was added dropwise with stirring until no further precipitation occurred. The precipitate was collected on a Buchner funnel, washed with water, and dried to afford H_4(olz) as an orange-yellow solid (1.492 g, 97.6%).

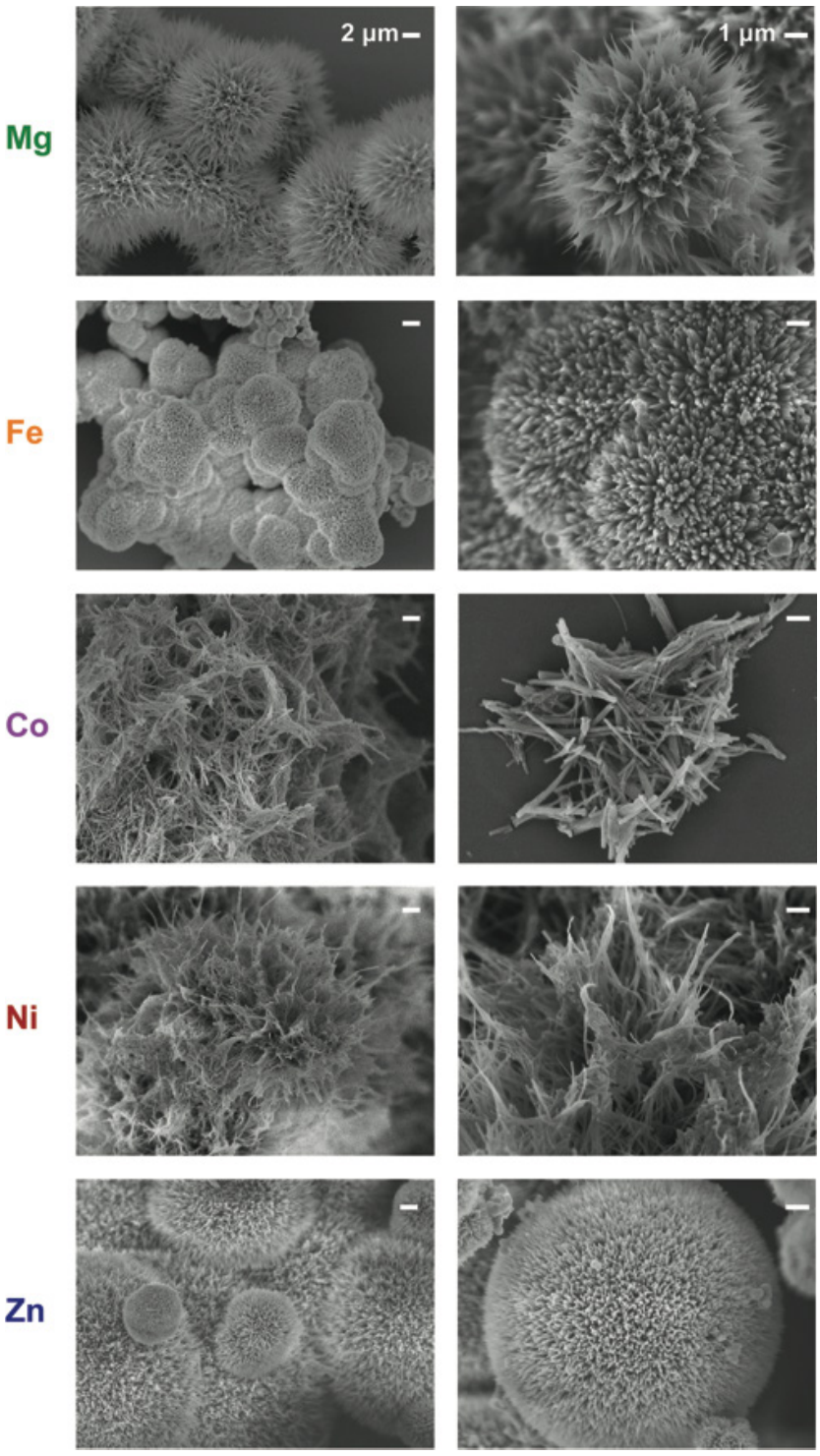

Figure S1. Scanning electron microscopy images of M_2(olz) crystallites (from top to bottom: Mg, Fe, Co, Ni, Zn; left column scale bars = 2 µm, right column scale bars = 1 µm). Images were taken using a JEOL JSM-6340F SEM. Samples were suspended in methanol and drop cast onto a silicon chip. To dissipate charge, the samples were sputter coated with approximately 3 nm of Au (Denton Vacuum).

II. Powder X-Ray Diffraction

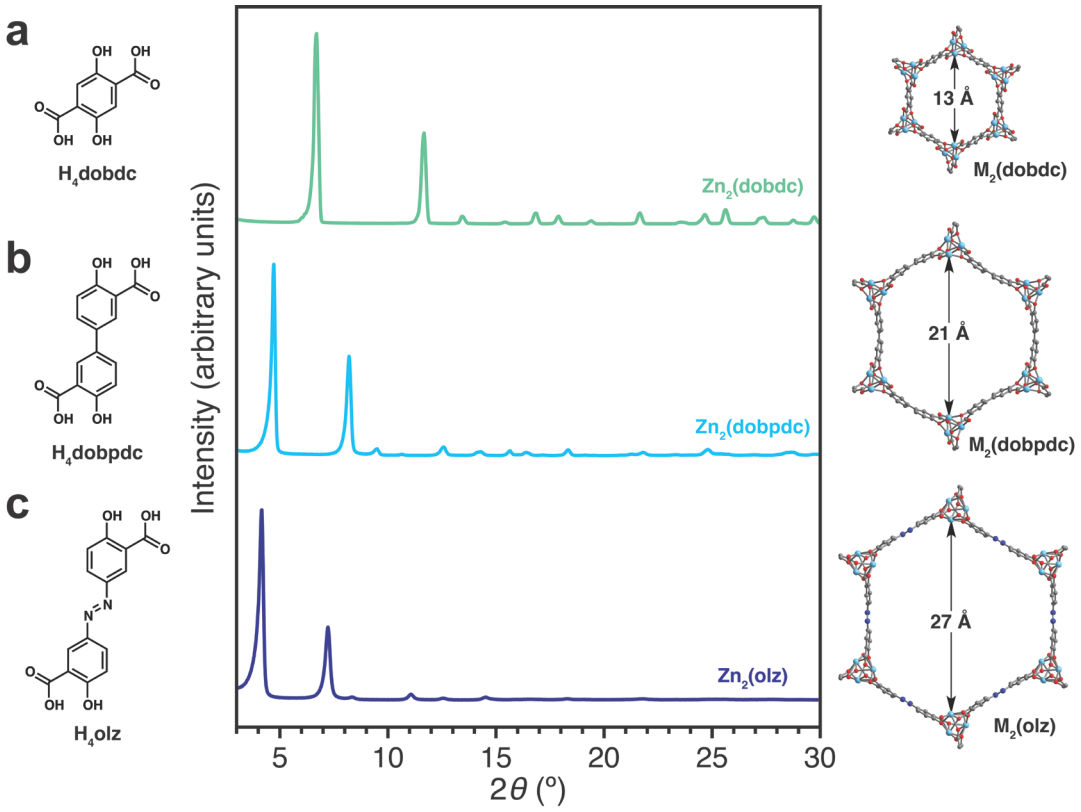

Figure S2. Comparison of isoreticular MOF-74 frameworks (a) M_2(dobdc), (b) M_2(dobpdc), and (c) M_2(olz). Left: structures of fully protonated ligands. Center: experimental powder X-ray diffraction patterns of Zn frameworks (λ = 1.5418 Å). Right: structural representations of desolvated frameworks with pore sizes indicated. Cyan, grey, red, and blue spheres correspond to metal, carbon, oxygen, and nitrogen atoms, respectively. Hydrogen atoms omitted for clarity.

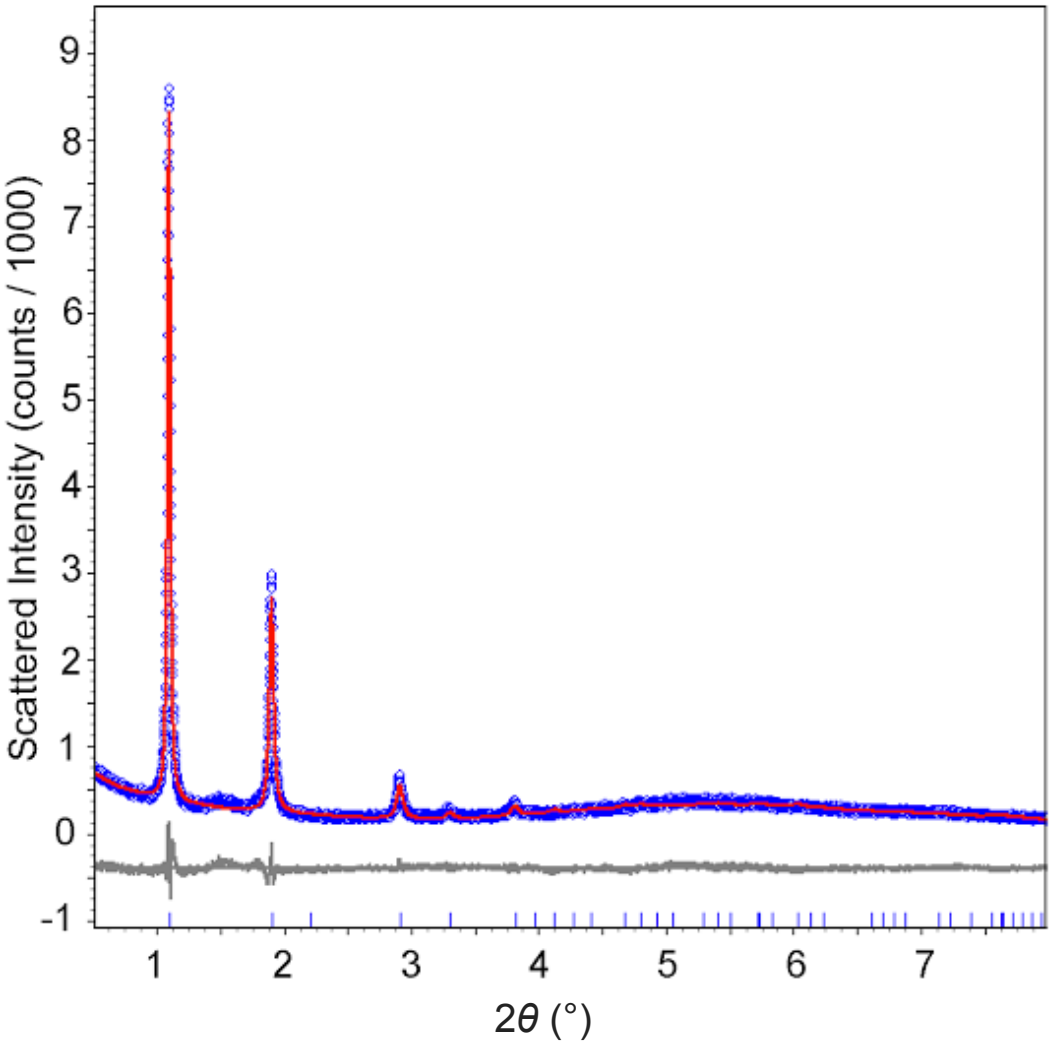

Figure S3. The observed scattered intensity for Mg_2(olz) is presented with blue circles, the best fit with a red line, and the difference plot with a gray line (λ = 0.414187 Å). The Bragg positions are given with vertical blue lines. During the refinement, the lattice and profile parameters were varied. Due to the poor quality of the diffraction data (only few reflections are observed, none of which corresponding to the *c*-axis), the structural model could not be refined. The model of the crystal structure was not refined and used as constructed in TOPAS (Figure S4), based on the related structure of Mg_2(dobpdc). The Rietveld refinement converged with the following figures of merit: R_{exp} = 0.0686, R_{exp}' = 0.1964, R_{wp} = 0.0821, R_{wp}' = 0.2352, R_p = 0.0643, R_p' = 0.2659, *GOF* = 1.98. The crystal structure was described in the $P3_221$ space group and the resulting unit cell parameters are a = 24.88(7) Å and c = 6.49(5) Å.

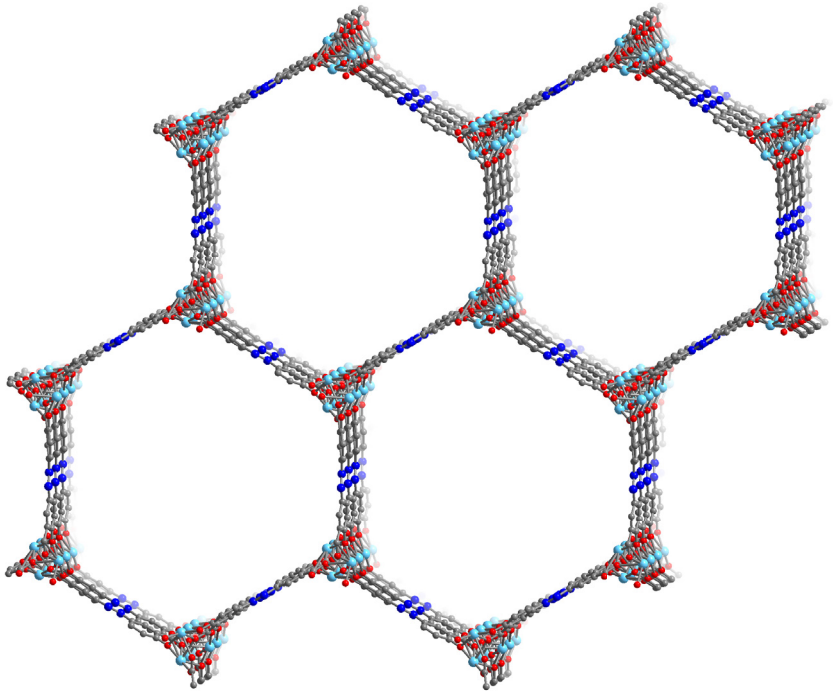

Figure S4. Structural model of M_2(olz) viewed down *c*-axis. Cyan, grey, red, and blue spheres correspond to metal, carbon, oxygen, and nitrogen atoms, respectively. Hydrogen atoms omitted for clarity.

Table S1. Pawley Fitting of the Unit Cell Parameters for M_2(olz) Frameworks from Powder X-Ray Diffraction.

	Mg_2(olz)	**Fe_2(olz)**	**Co_2(olz)**	**Ni_2(olz)**	**Zn_2(olz)·EtOH$_x$**
λ / Å	0.72768	0.72768	0.72768	0.72768	0.72768
T / K	273	273	273	273	273
Space group	$P3_221$	$P3_221$	$P3_221$	$P3_221$	$P3_221$
***a* / Å**	24.97(5)	25.03(4)	24.81(5)	24.91(4)	25.42(6)
***c* / Å**	6.72(4)	6.53(7)	6.63(5)	6.65(7)	6.84(6)
***V* / Å^3**	3629(2)	3543(4)	3534(3)	3570(4)	3824(3)
R_{exp}	1.312	0.877	1.688	1.228	1.400
R_{wp}	2.928	4.042	3.563	3.766	3.211
R_p	2.089	2.507	2.020	2.695	2.040

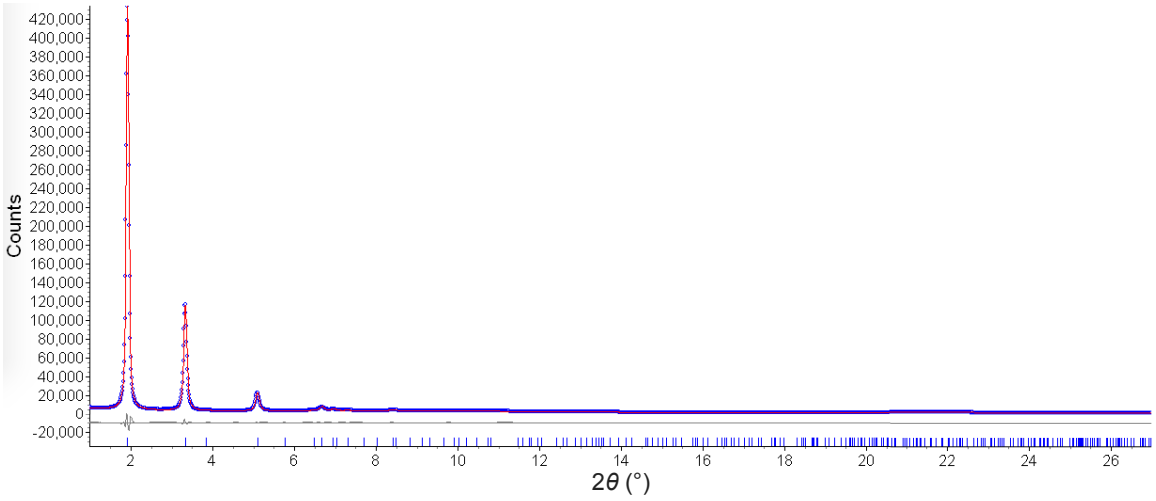

Figure S5. Pawley fit for Mg_2(olz) showing the observed (blue) and fitted (red) powder X-ray diffraction patterns and the difference (grey) (λ = 0.72768 Å).

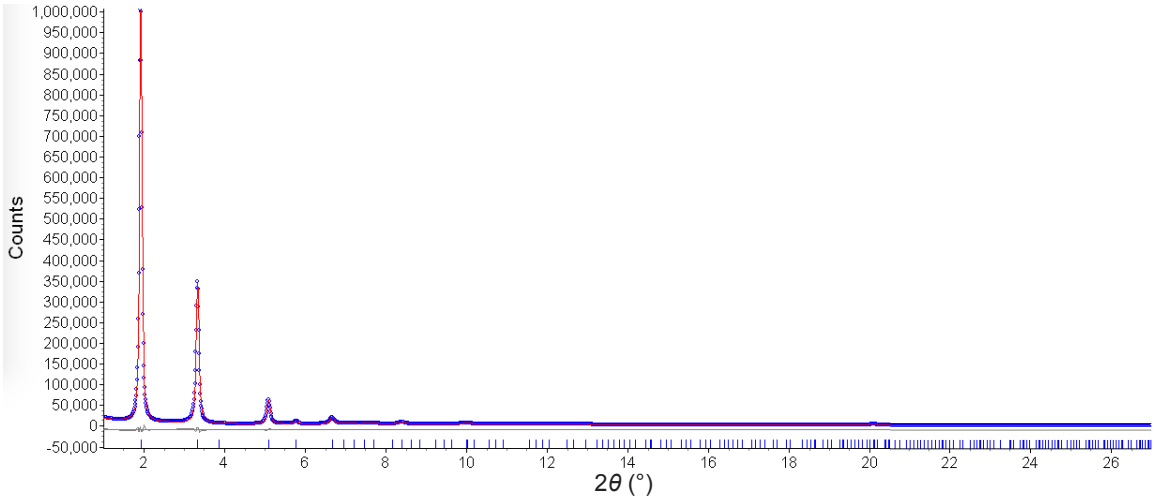

Figure S6. Pawley fit for Fe_2(olz) showing the observed (blue) and fitted (red) powder X-ray diffraction patterns and the difference (grey) (λ = 0.72768 Å).

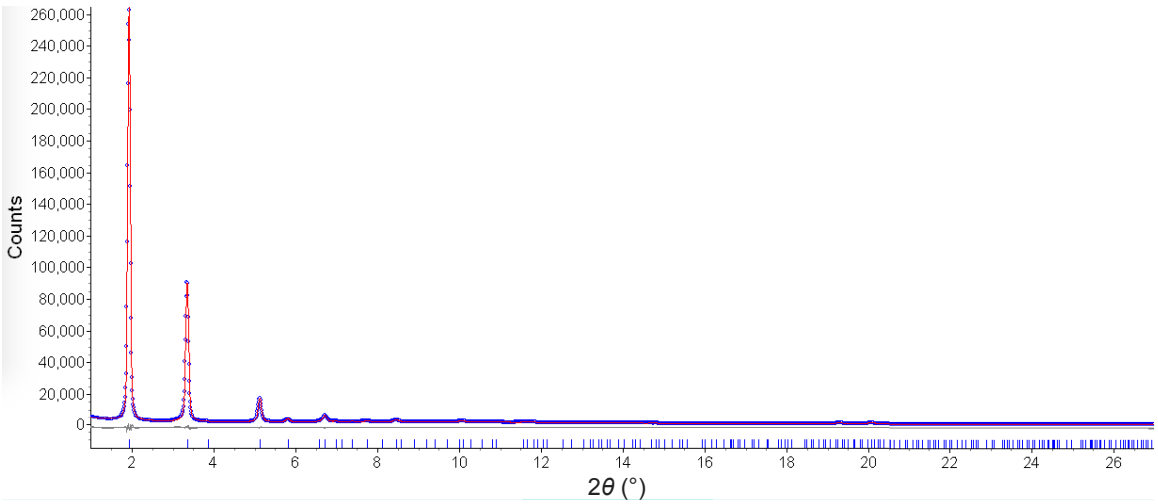

Figure S7. Pawley fit for Co_2(olz) showing the observed (blue) and fitted (red) powder X-ray diffraction patterns and the difference (grey) (λ = 0.72768 Å).

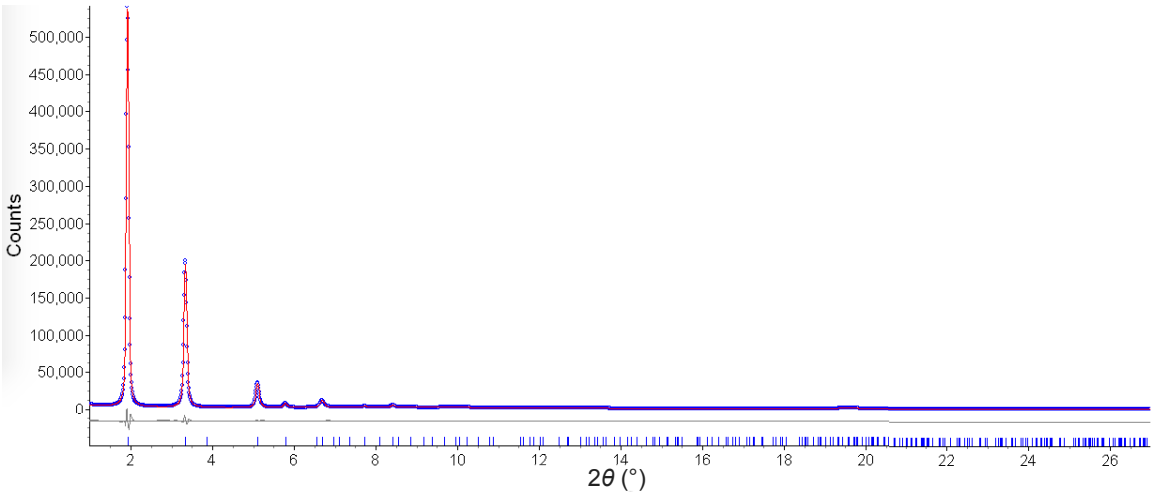

Figure S8. Pawley fit for Ni_2(olz) showing the observed (blue) and fitted (red) powder X-ray diffraction patterns and the difference (grey) (λ = 0.72768 Å).

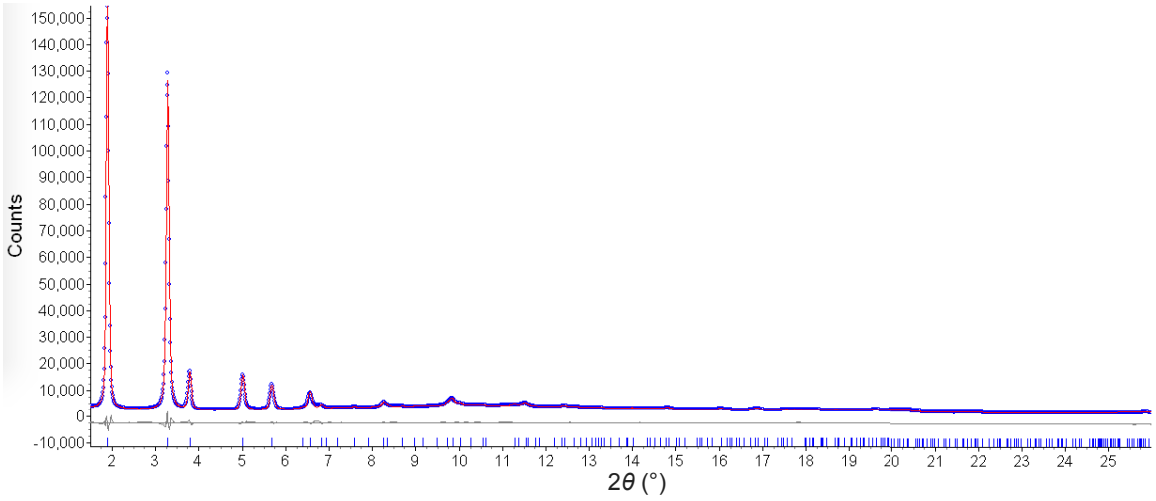

Figure S9. Pawley fit for ethanol-solvated Zn_2(olz) showing the observed (blue) and fitted (red) powder X-ray diffraction patterns and the difference (grey) (λ = 0.72768 Å).

III. N_2 Adsorption Isotherms and Surface Area Calculations

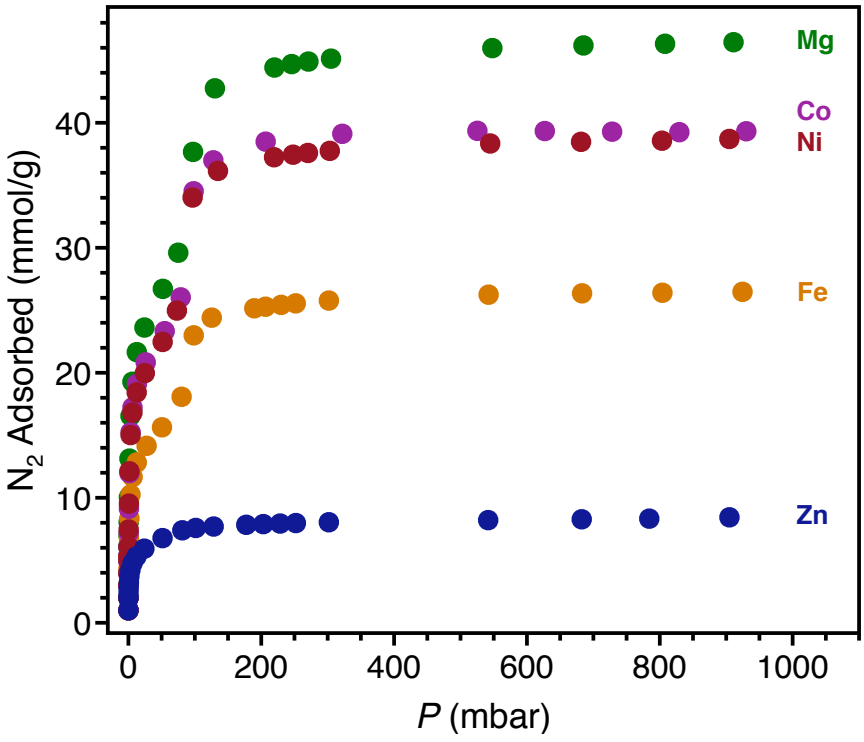

Figure S10. Isotherms for the adsorption of N_2 at 77 K in activated M_2(olz) (From top: M = Mg, Co, Ni, Fe, Zn).

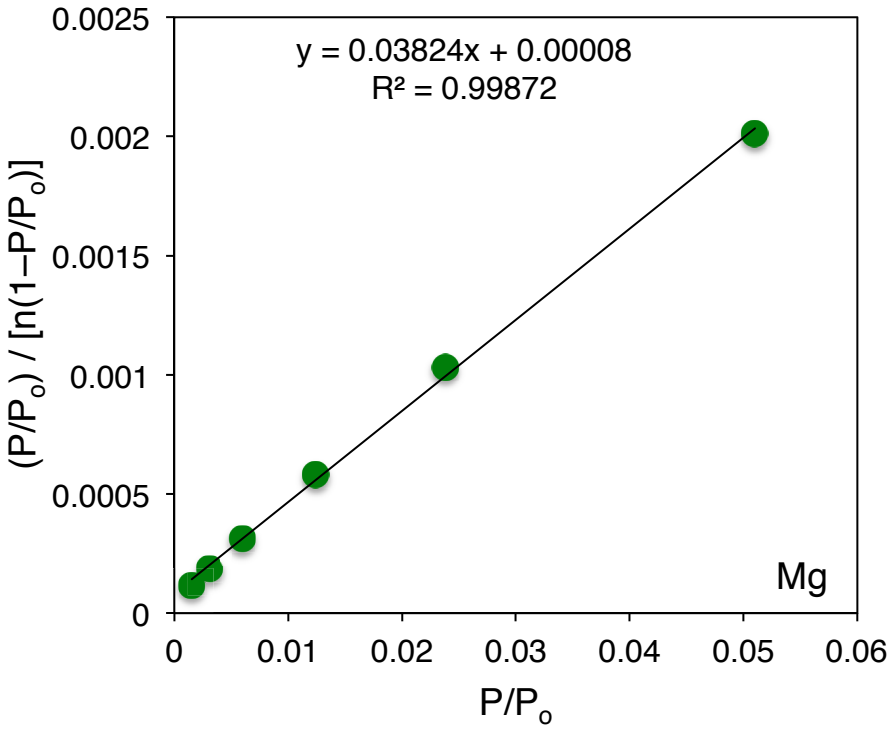

Figure S11. Linear plot for Mg_2(olz) BET calculation.

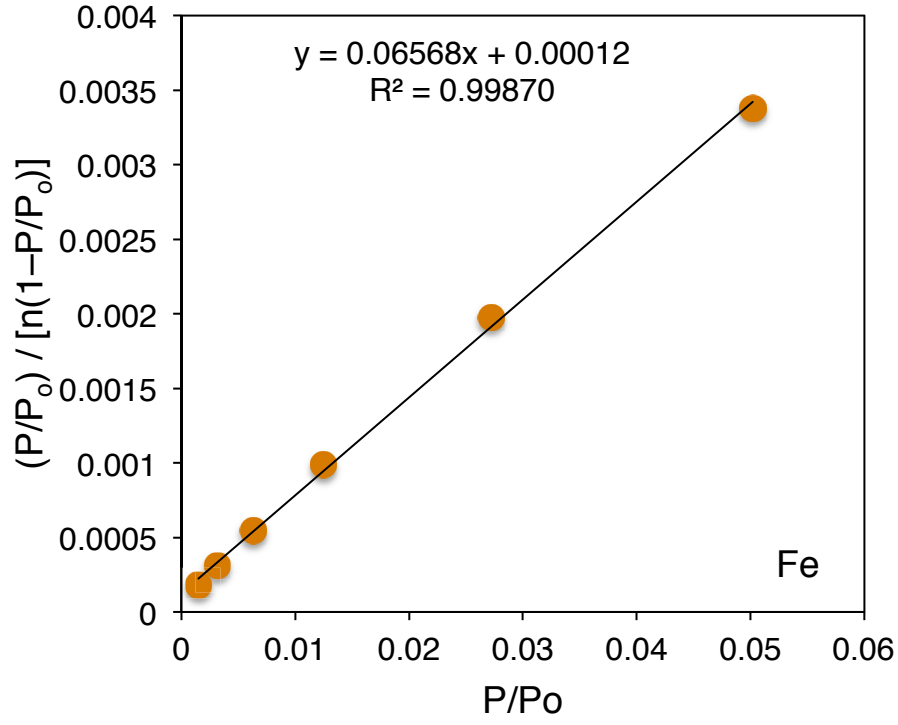

Figure S12. Linear plot for Fe_2(olz) BET calculation.

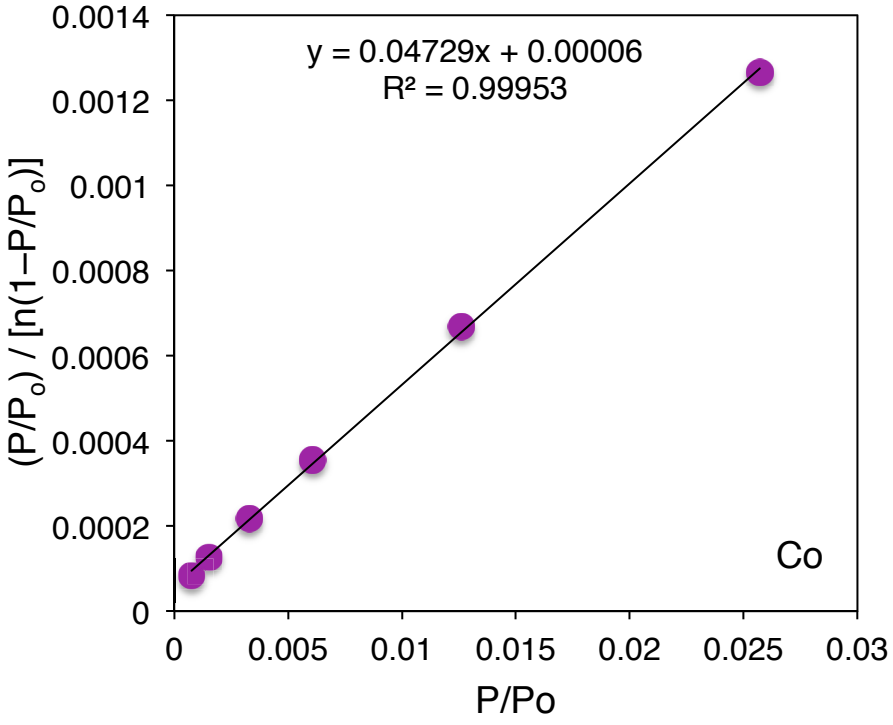

Figure S13. Linear plot for Co_2(olz) BET calculation.

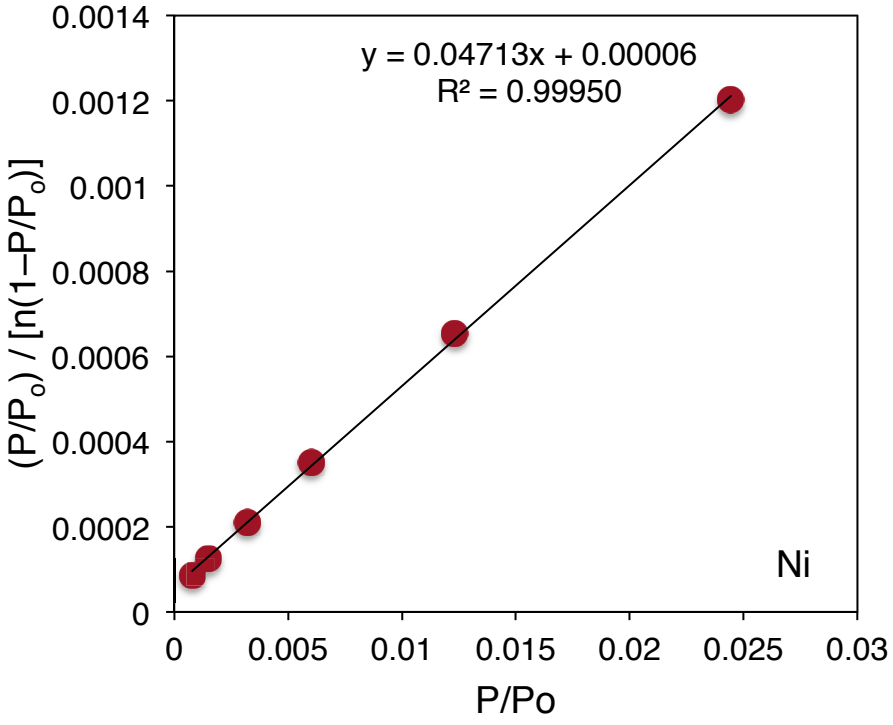

Figure S14. Linear plot for Ni_2(olz) BET calculation.

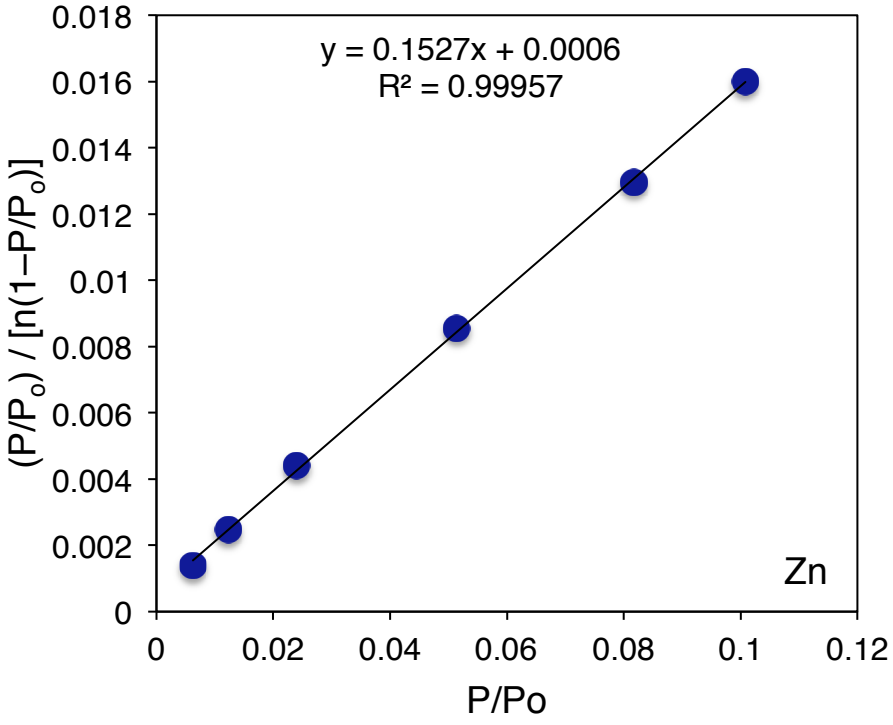

Figure S15. Linear plot for Zn_2(olz) BET calculation.

IV. H_2 Adsorption Isotherms

The dual-site Langmuir−Freundlich expression (Equation S1) was used to fit the combined isotherm data at 77 K and 87 K for Mg_2(olz), Fe_2(olz), Ni_2(olz), and Zn_2(olz). The tri-site Langmuir expression (Equation S2) was used to fit the data for Co_2(olz), where n is the amount of gas adsorbed (mmol/g), q_{sat} is the saturation loading for site 1, 2, or 3 (mmol/g), b is the Langmuir parameter associated with either site 1, 2, or 3 (bar^{-v}), p is the pressure, and v is a constant. The value for b is calculated per Equation S3.

$$n = \frac{q_{sat,1} b_1 p^{v_1}}{1 + b_1 p^{v_1}} + \frac{q_{sat,2} b_2 p^{v_2}}{1 + b_2 p^{v_2}} \qquad \text{Equation S1}$$

$$n = \frac{q_{sat,1} b_1 p^{v_1}}{1 + b_1 p^{v_1}} + \frac{q_{sat,2} b_2 p^{v_2}}{1 + b_2 p^{v_2}} + \frac{q_{sat,3} b_3 p^{v_3}}{1 + b_3 p^{v_3}} \qquad \text{Equation S2}$$

$$b_i = e^{-S_i} e^{E_i \cdot 1000/RT} \qquad \text{Equation S3}$$

The equation was fit using the statistical software package of OriginPro 8. The quality of fits was determined by comparing the adjusted R^2 and residual sum of squares values, as well as by visual inspection. Wolfram Mathematica 7 was then used to create a series of data points corresponding to points on the fit curve. The isosteric heat of adsorption Q_{st} was then calculated using the data points from Mathematica for both the 77 K and 87 K isotherms using the Clausius-Clapeyron relation (Equation S4) at equivalent loadings (n, mmol/g). Q_{st} is the isosteric heat of adsorption (kJ/mol), R is the gas constant (L*bar/[mol*K]), and P is the pressure at a given n at either T_2 (87 K) or T_1 (77 K).

$$Q_{st} = -\frac{R\left[\ln(P_{T_2}) - \ln(P_{T_2})\right]}{T_2^{-1} - T_1^{-1}} \qquad \text{Equation S4}$$

Table S2. Dual and tri-site Langmuir fit parameters for the H_2 isotherms for M_2(olz) in Figures S16-S20.

	Mg_2(olz)	Fe_2(olz)	Co_2(olz)	Ni_2(olz)	Zn_2(olz)
$q_{sat,1}$ (mmol/g)	4.36	2.66	4.19	4.04	0.74
S_1 (R)	9.57	10.52	10.28	9.96	8.86
E_1 (kJ/mol)	10.29	10.38	11.63	12.10	8.04
v_1	0.95	1	1.03	1	1
$q_{sat,2}$ (mmol/g)	29.14	21.52	20.49	14.06	4.72
S_2 (R)	7.46	10.07	6.94	7.92	7.01
E_2 (kJ/mol)	3.88	5.50	3.62	4.73	4.56
v_2	0.86	0.76	0.97	1	1
$q_{sat,3}$ (mmol/g)	–	–	1.53	–	–
S_3 (R)	–	–	16.38	–	–
E_3 (kJ/mol)	–	–	11.05	–	–
v_3	–	–	0.62	–	–

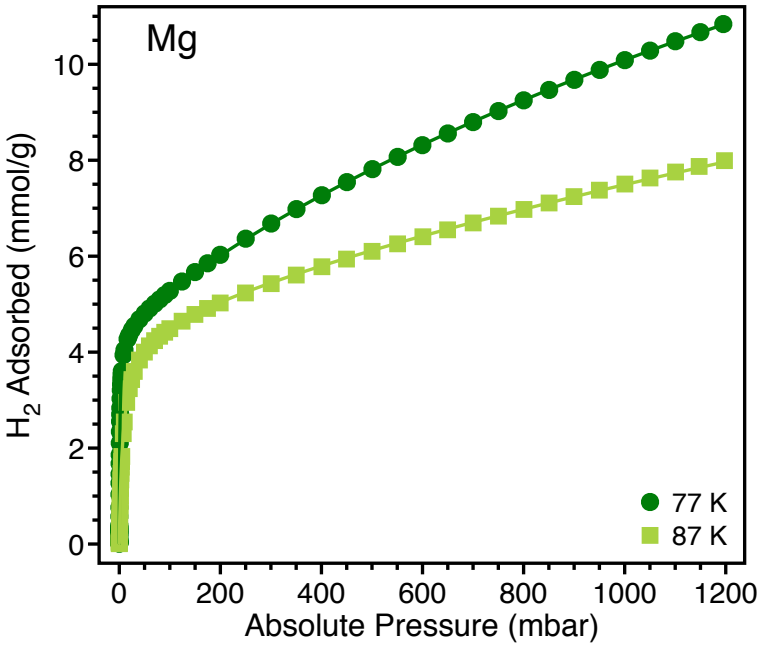

Figure S16. H_2 adsorption isotherms at 77 K and 87 K for Mg_2(olz). The solid lines represent the simultaneous dual-site Langmuir fit to the data, using the parameters given in Table S2.

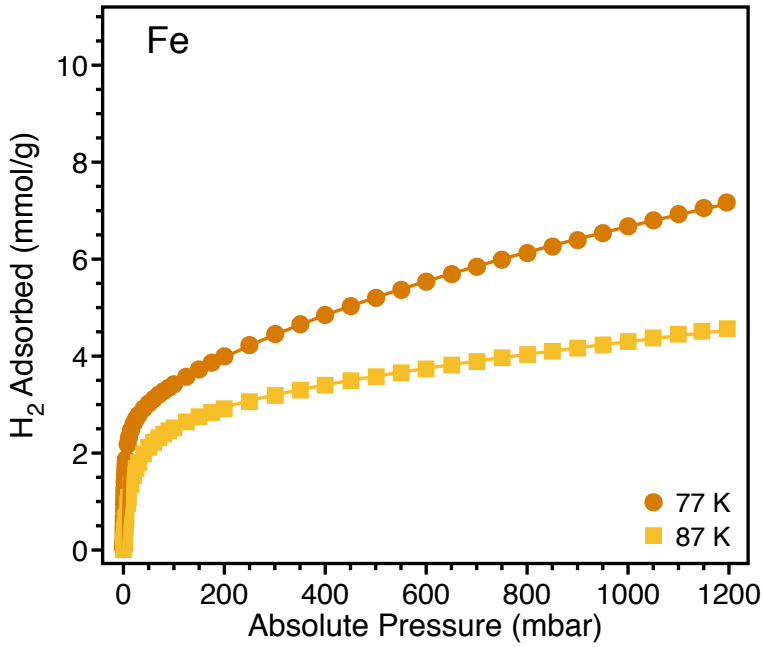

Figure S17. H_2 adsorption isotherms at 77 K and 87 K for Fe_2(olz). The solid lines represent the simultaneous dual-site Langmuir fit to the data, using the parameters given in Table S2.

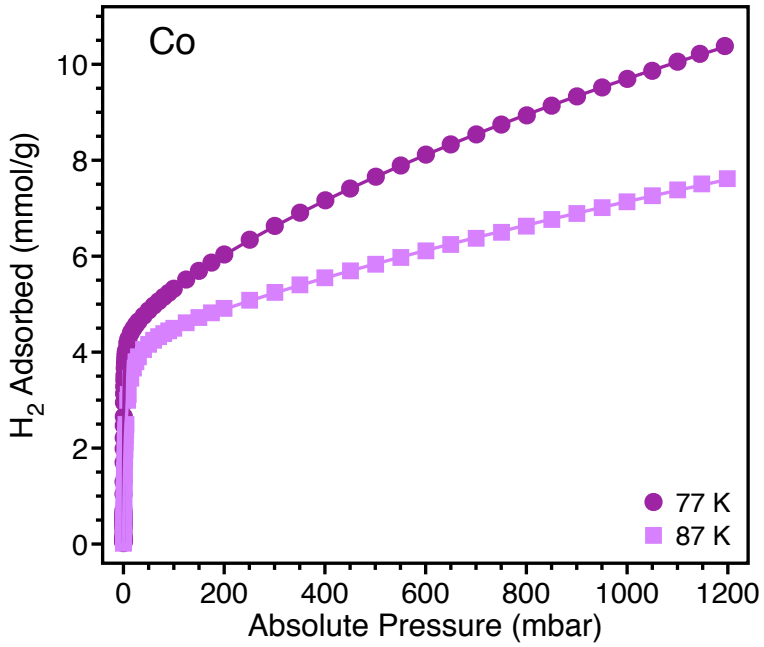

Figure S18. H_2 adsorption isotherms at 77 K and 87 K for Co_2(olz). The solid lines represent the simultaneous tri-site Langmuir fit to the data, using the parameters given in Table S2.

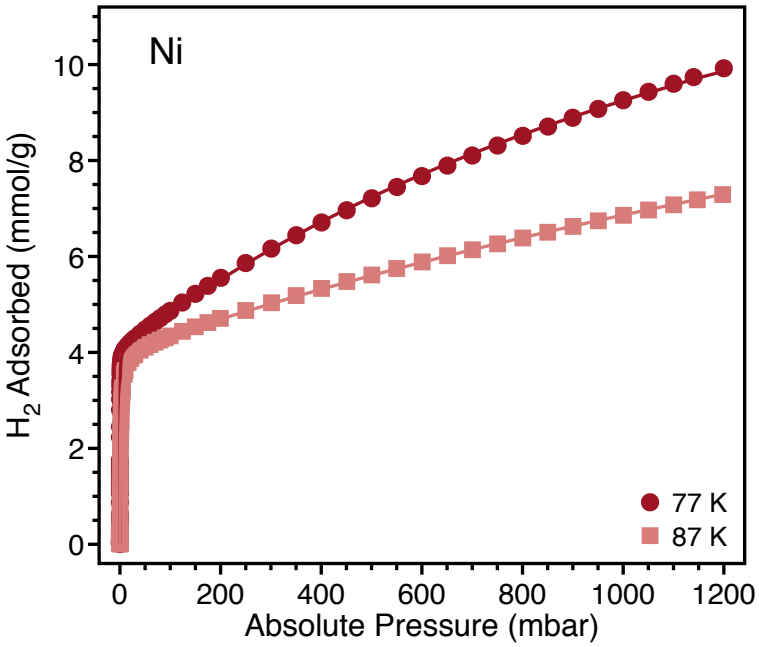

Figure S19. H_2 adsorption isotherms at 77 K and 87 K for Ni_2(olz). The solid lines represent the simultaneous dual-site Langmuir fit to the data, using the parameters given in Table S2.

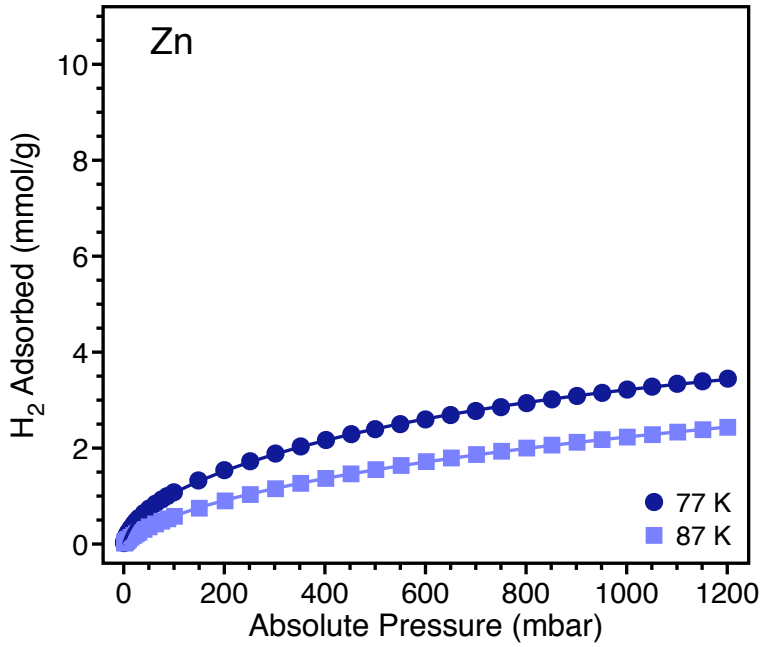

Figure S20. H_2 adsorption isotherms at 77 K and 87 K for Zn_2(olz). The solid lines represent the simultaneous dual-site Langmuir fit to the data, using the parameters given in Table S2.

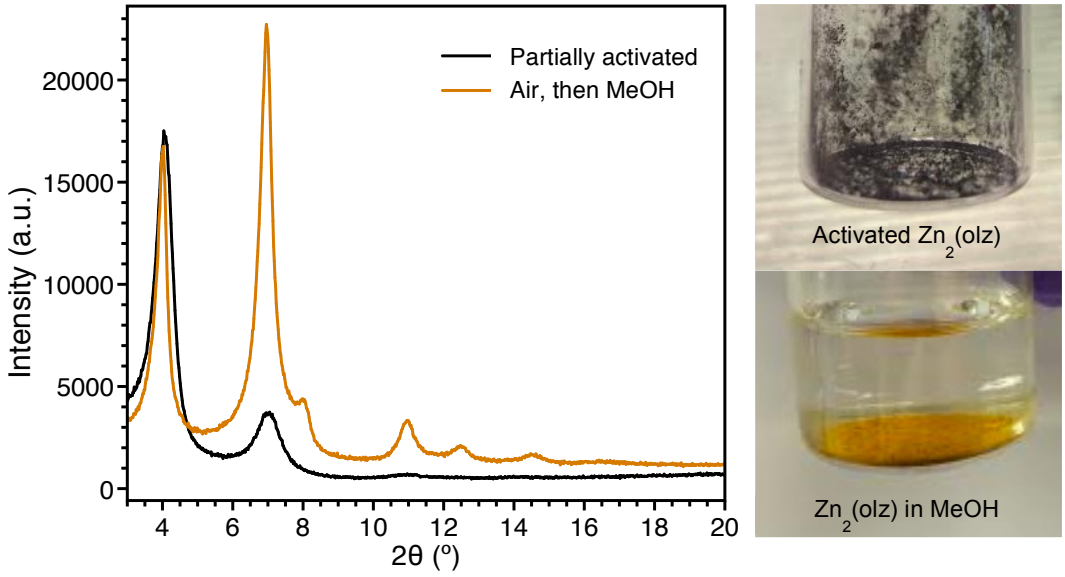

Figure S21. Decreased crystallinity of Zn_2(olz) after partial activation at 65 °C is regained after exposure to methanol by powder X-ray diffraction (λ = 1.5418 Å). This behavior is suggestive of framework collapse upon desolvation, resulting in loss of long-range order and decreased surface area. When re-immersed in a coordinating solvent such as methanol, crystallinity is restored.

V. Thermogravimetric Analysis

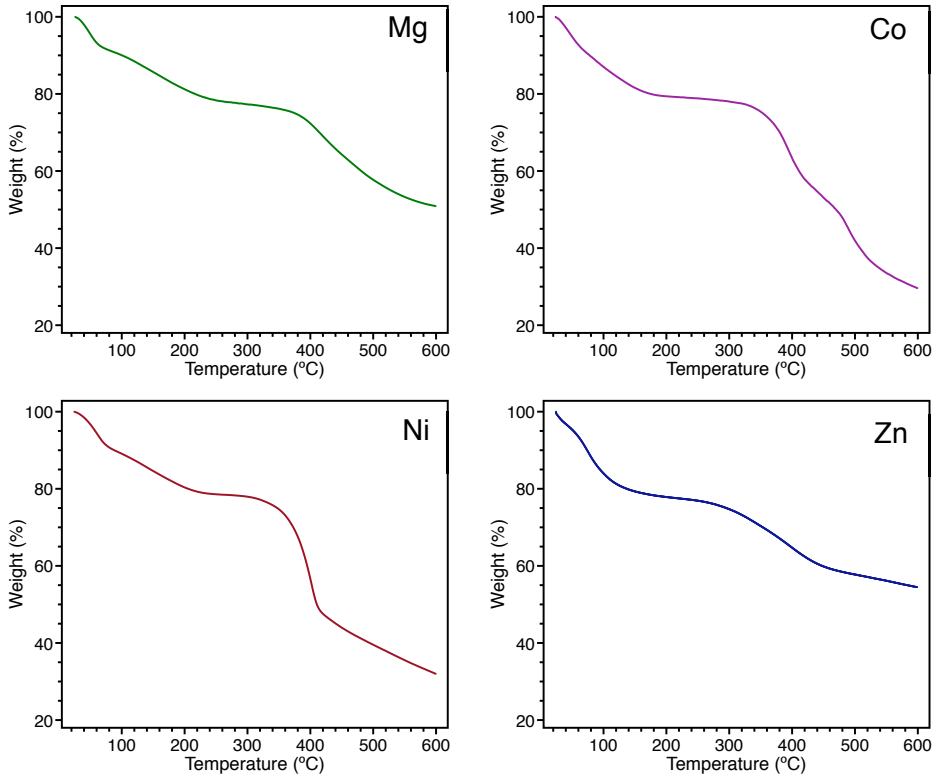

Figure S22. Thermogravimetric analysis (TGA) of air-stable methanol-solvated M_2(olz) frameworks. Data collected with a ramp rate of 2 °C/min.

VI. *In Situ* Infrared Spectroscopy

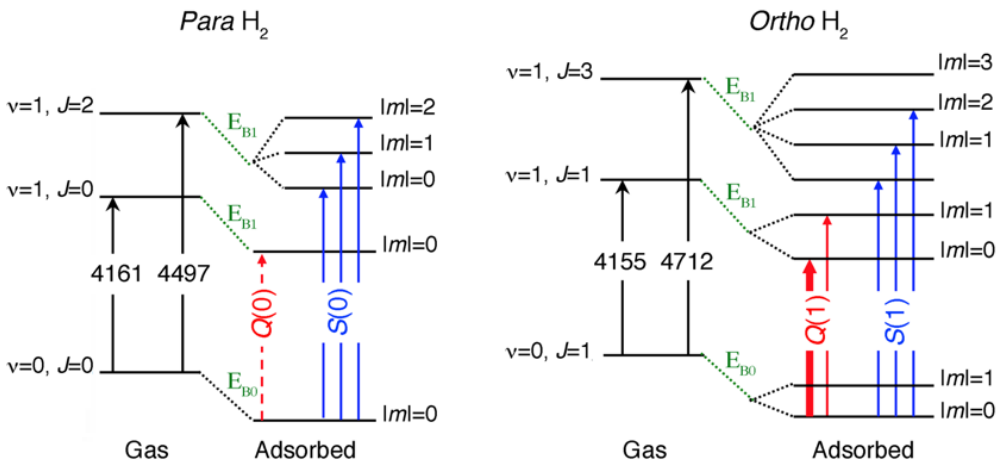

Figure S23. Energy diagram of molecular hydrogen explaining the vibrational transitions observed in metal–organic frameworks. While gas phase H_2 is not observed by IR spectroscopy, the polarization of the molecule upon interaction with a metal cation results in transitions from the vibrational ground state ($v = 0$) to the first excited state ($v = 1$) for *para* and *ortho*-H_2. J is the rotational quantum number. The values indicate gas phase transition frequency in cm^{-1}. Dashed vertical arrows indicate transitions that are activated by the overlap mechanism, solid arrows indicate the quadrupole mechanism, and the transition marked with the thick arrow is activated by both. E_{B0} and E_{B1} are the binding energies in the ground state and vibrationally excited states, respectively.

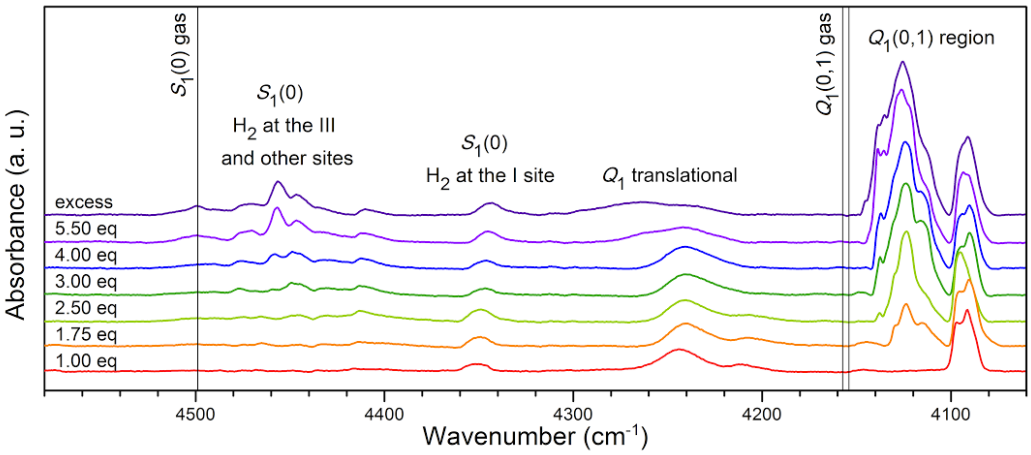

Figure S24. H_2 adsorbed at multiple binding sites as a function of loading in Mg_2(olz). IR absorption of H_2 at 15 K, the equivalent number refers to H_2 molecules per Mg. The vertical lines show the H_2 gas phase wavenumber values for vibration (Q) and vibration-rotation (S) excitations. Q_1 translational refers to the center-of-mass motion of the adsorbed H_2. Q(0) and S(0) refer to *para*-H_2 and Q(1) to *ortho*-H_2. Subscript 1 indicates fundamental transition in which the vibrational quantum number increases by one.

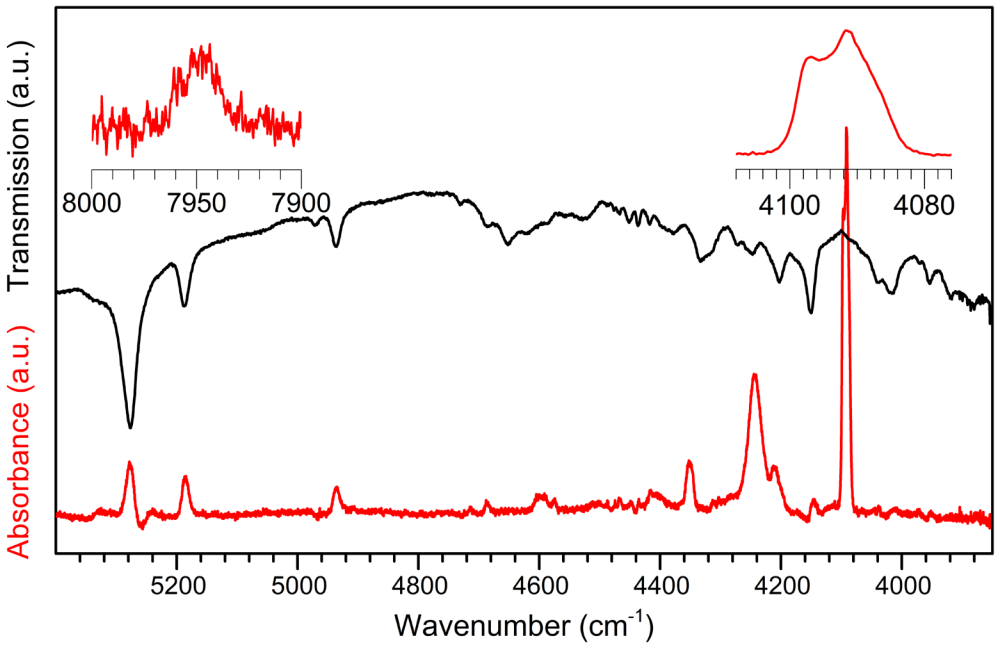

Figure S25. H_2 adsorbed at an open metal site. Curve in red: absorbance at 15 K for one H_2 per Mg relative to activated sample of Mg_2(olz). Insets: overtone and fundamental stretching vibrations of H_2, showing peaks of both *ortho* and *para* hydrogen. Curve in black: Raw IR signal for activated Mg_2(olz) sample at 15 K.

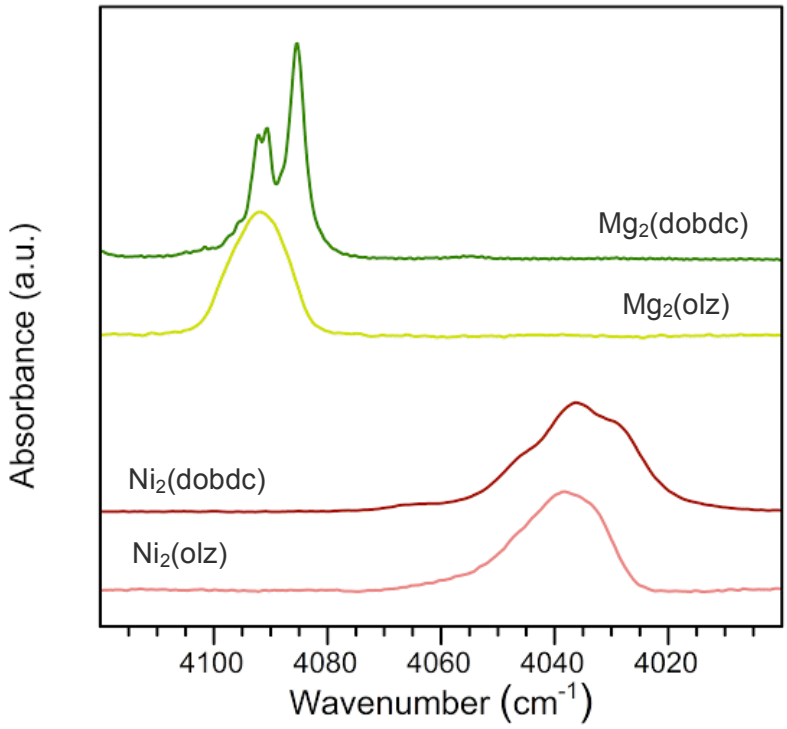

Figure S26. IR spectra of H_2 adsorbed at an open metal site, recorded at 77 K. Mg_2(dobdc), Mg_2(olz), Ni_2(dobdc), and Ni_2(olz) (dobdc^{4-} = 2,5-dioxido-1,4-benzenedicarboxylate) loaded with one H_2 molecule per open metal site. For frameworks composed of the same metal but different organic linker, the similar wavenumber values for the H_2 stretching vibrations indicate similar local environment around the metal center. The observed redshifts in the nickel frameworks indicate that H_2 is more strongly bound to the nickel open metal sites than the analogous magnesium sites; this is confirmed by the calculated entropy and enthalpy changes upon adsorption. The small difference in the redshift of bound H_2 between the dobdc^{4-} and the olz^{4-} analogues is consistent with similar binding energies observed in previously reported plots of isosteric heats of adsorption.[1,2]

1. Sumida, K.; Brown, C. M.; Herm, Z. R.; Chavan, S.; Bordiga, S.; Long, J. R. *Chem. Commun.* **2011**, *47* (4), 1157.

2. Kapelewski, M. T.; Geier, S. J.; Hudson, M. R.; Stück, D.; Mason, J. A.; Nelson, J. N.; Xiao, D. J.; Hulvey, Z.; Gilmour, E.; FitzGerald, S. A.; Head-Gordon, M.; Brown, C. M.; Long, J. R. *J. Am. Chem. Soc.* **2014**, *136* (34), 12119.

VII. Drug Loading and Release in Mg_2(olz)

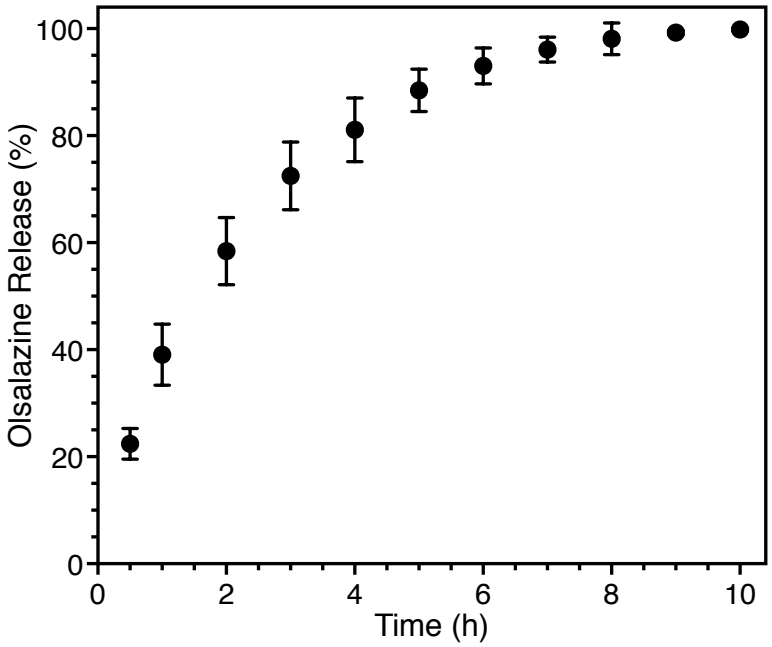

Figure S27. Olsalazine release from Mg_2(olz). Pellets were prepared from a circular die with a 4 mm diameter and pressed in a vise under a consistent pressure to produce 4.0 (± 0.3) mg pellets. The release experiments were carried out under simulated biological conditions where each pellet was placed in a 50 mL conical tube with 30 mL of phosphate-buffered saline (PBS). The tubes were oriented horizontally in the shaking incubator at 37 °C with bidimensional stirring at 60 rpm. Aliquots of 200 μL were removed at every time point, and 75 μL of each sample were transferred to a clear-bottom 96-well plate in duplicate and calibrated against Na_2(olz) standards in PBS at known concentrations. Absorbance was measured at 360 nm by a Molecular Devices SpectraMax Paradigm plate reader.

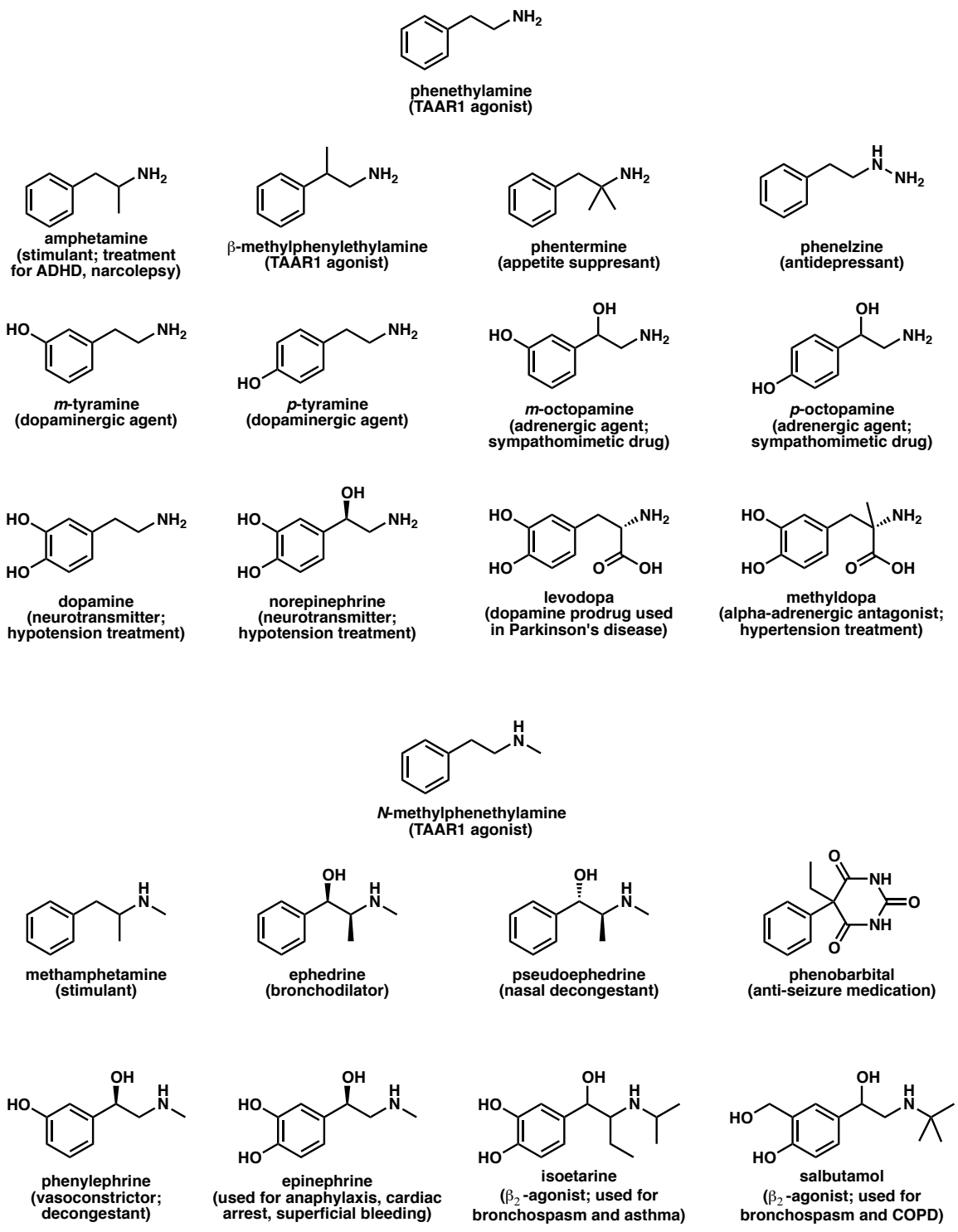

Figure S28. A selection of primary and secondary phenethylamine derivatives of pharmaceutical importance.

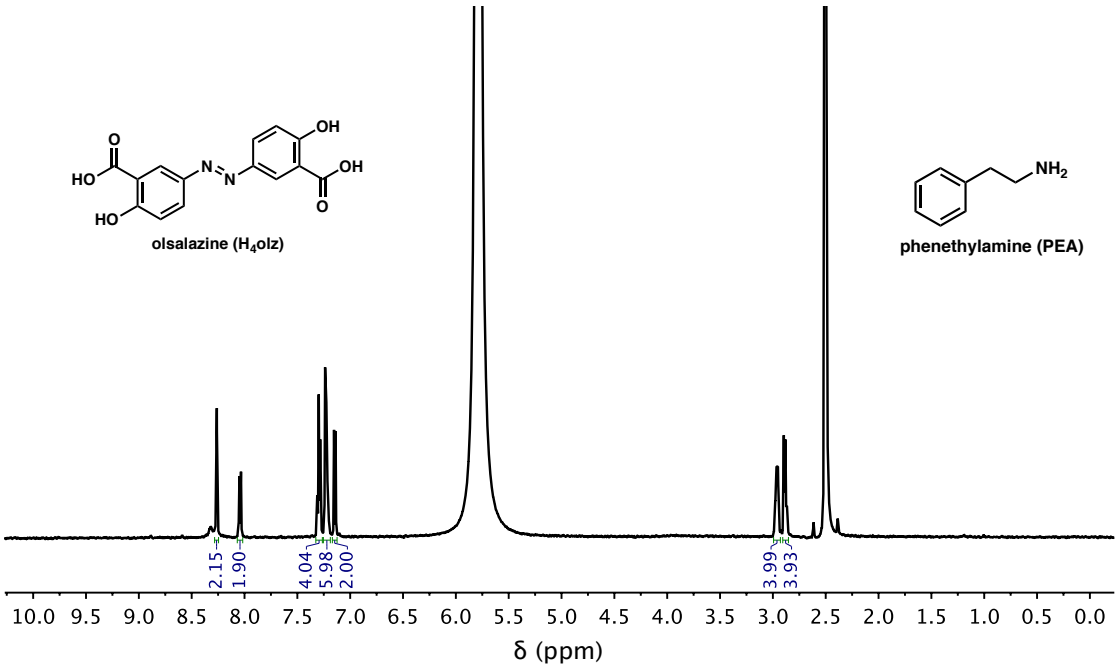

Figure S29. Digestion of $Mg_2(olz)(PEA)_2$ in DMSO-d_6 (530 µL) and DCl (20 µL). ^{1}H NMR (600 MHz, DMSO-d_6): olsalazine δ 8.26 (d, J = 2.5 Hz, 2H), 8.04 (dd, J = 8.9, 2.5 Hz, 2H), 7.15 (d, J = 8.9 Hz, 2H); phenethylamine 7.30 (t, J = 7.5 Hz, 4H), 7.22 (dd, J = 12.0, 7.3 Hz, 6H), 2.96 (d, J = 8.1 Hz, 4H), 2.91 – 2.85 (m, 4H).

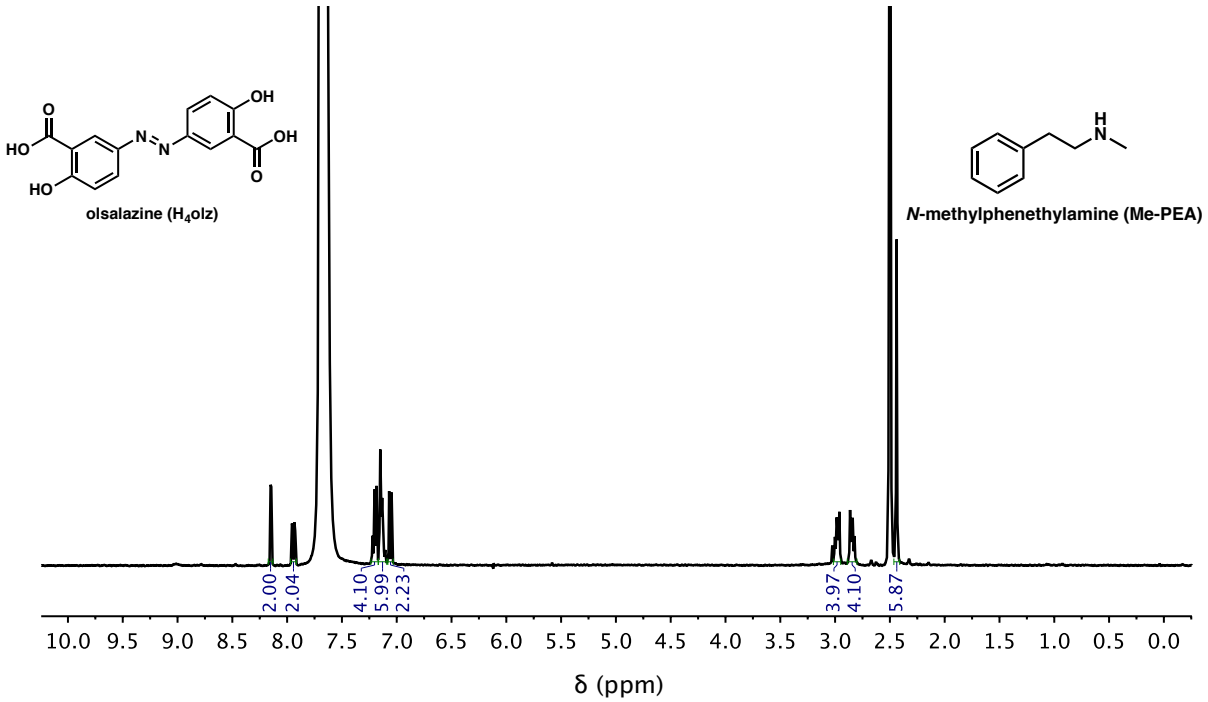

Figure S30. Digestion of Mg_2(olz)(Me-PEA)$_2$ in DMSO-d_6 (530 µL) and DCl (70 µL). ^{1}H NMR (400 MHz, DMSO-d_6): olsalazine δ 8.15 (d, J = 2.5 Hz, 2H), 7.94 (dd, J = 8.9, 2.5 Hz, 2H), 7.06 (d, J = 8.9 Hz, 2H); *N*-methylphenethylamine δ 7.23 – 7.17 (m, 4H), 7.14 (dd, J = 7.6, 3.6 Hz, 6H), 2.98 (dd, J = 10.3, 5.9 Hz, 4H), 2.84 (dd, J = 10.3, 5.9 Hz, 4H), 2.44 (s, 6H).

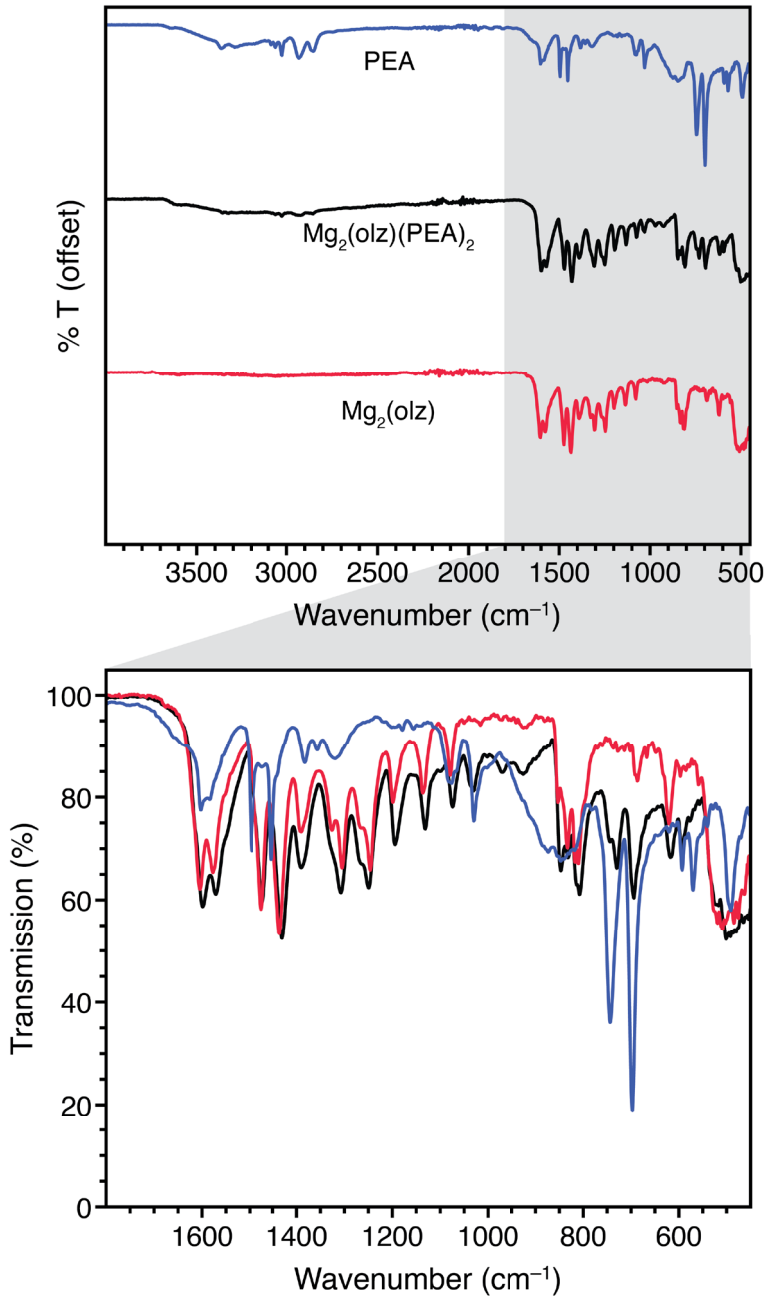

Figure S31. Infrared spectra of phenethylamine (blue), $Mg_2(olz)(PEA)_2$ (black), and $Mg_2(olz)$ (red). It is apparent that the IR spectrum of $Mg_2(olz)(PEA)_2$ does not present a simple superposition of the $Mg_2(olz)$ and PEA IR spectra. The changes in the fingerprint region indicate interaction of the $Mg_2(olz)$ framework and adsorbed PEA in the solid state.